CCFE
CULHAM CENTRE FOR FUSION ENERGY

UK Atomic Energy Authority

UKAEA-CCFE-CP(20)121

S. S. Henderson, M. Bernert, C. Giroud, D. Brida, M. Cavedon, P. David, R. Dux, J. R. Harrison, A. Huber, A. Kallenbach, J. Karhunen, B. Lomanowski, G. Matthews, A. Meigs, R. A. Pitts, F. Reimold, M. L. Reinke, S. Silburn, N. Vianello, S. Wiesen, M. Wischmeier

# Parameter dependencies of the experimental nitrogen concentration required for detachment on ASDEX Upgrade and JET

# Parameter dependencies of the experimental nitrogen concentration required for detachment on ASDEX Upgrade and JET

S. S. Henderson, M. Bernert, C. Giroud, D. Brida, M. Cavedon, P. David, R. Dux, J. R. Harrison, A. Huber, A. Kallenbach, J. Karhunen, B. Lomanowski, G. Matthews, A. Meigs, R. A. Pitts, F. Reimold, M. L. Reinke, S. Silburn, N. Vianello, S. Wiesen, M. Wischmeier

This paper has been submitted to
24th International Conference on Plasma Surface Interactions in Controlled Fusion Devices (PSI), South Korea, 24 - 29 January 2021

# Parameter dependencies of the experimental nitrogen concentration required for detachment on ASDEX Upgrade and JET

S. S. Henderson[a], M. Bernert[b], C. Giroud[a], D. Brida[b], M. Cavedon[b], P. David[b], R. Dux[b], J. R. Harrison[a], A. Huber[c], A. Kallenbach[b], J. Karhunen[e], B. Lomanowski[d], G. Matthews[a], A. Meigs[a], R. A. Pitts[f], F. Reimold[g], M. L. Reinke[d], S. Silburn[a], N. Vianello[h], S. Wiesen[c], M. Wischmeier[b], the EUROfusion MST1 team[1], ASDEX Upgrade team[2], and JET contributors[3]

[a]*CCFE, Culham Science Centre, Abingdon, OX14 3DB, UK*
[b]*Max-Plank-Institut für Plasmaphysik, D-85748 Garching, Germany*
[c]*Forschungszentrum Jülich GmbH, Institut für Energie-und Klimaforschung, 52425 Jülich, Germany*
[d]*Oak Ridge National Laboratory, Oak Ridge, TN 37831, USA*
[e]*Aalto University, Department of Applied Physics, 02150 Espoo, Finland*
[f]*ITER Organization, Route de Vinon-sur-Verdon, CS 90 046, 13067 St. Paul Lez Durance Cedex, France*
[g]*Max-Plank-Institut für Plasmaphysik, 17489 Greifswald, Germany*
[h]*Consorzio RFX (CNR, ENEA, INFN, Universita di Padova), Corso Stati Uniti 4, 35127 Padova, Italy*

**Abstract**

While current tokamak experiments are beginning to utilise real-time feedback control systems to manage the plasma exhaust, future tokamaks still require validation of theoretical models used to predict the threshold impurity concentration required to facilitate stationary divertor operation. This work exploits new spectroscopic measurements of the divertor nitrogen concentration, $c_N$, in $N_2$ seeded H-mode ASDEX Upgrade and JET plasmas to test the parameter dependencies of the power flowing to the outer divertor, $P_{div,outer}$, the separatrix density, $n_{e,sep}$, the plasma current, $I_P$, and the minor radius, $a_{min}$. An experimental scaling law to predict the threshold $c_N$ required for detachment which best fits the experimental data from both devices is $c_N \propto P_{div,outer}^{1.06\pm0.28} n_{e,sep}^{-2.67\pm0.27} I_P^{0.97\pm0.36} a_{min}^{-1.99\pm0.25}$. The dependency of $P_{div,outer}$ and $n_{e,sep}$ is demonstrated over at least a factor of two change in both parameters and indicates a moderately stronger dependence on $n_{e,sep}$ in comparison to the Lengyel model. This first assessment of the machine size scaling highlights the need for similar measurements from other tokamaks to validate the results.

*Keywords:* impurity, nitrogen, divertor, concentration, spectroscopy, tokamak, seeding

## 1. Introduction

Reducing the power and particle fluxes impacting on the divertor targets is one of the key challenges facing future fusion experiments. One of the main techniques to achieve this is through substantial seeding of impurities, such as $N_2$, Ne, or Ar, which will be utilised on ITER to facilitate stationary divertor operation [1]. Despite impurity seeding being used for many years and on many different tokamaks [2–7], direct measurements of the seeding gas concentration are limited [8, 9]. Recently, control of the divertor detachment state has been reliably demonstrated using real-time feedback control on divertor measurements (e.g. shunt currents measuring the outer divertor temperature [10], AXUV diodes measuring the X-point radiation location [11], or filtered cameras tracking the C III front position [12]) whilst using the fuelling and seeding gas valve fluxes as actuators. This effectively removes the need for any detailed understanding of the required impurity concentration. However, future tokamaks, like ITER and DEMO, rely on validated predictions of the impurity concentration to ensure an integrated scenario compatible with both the core and edge plasma.

Attempts to predict the impurity concentration have been made using sophisticated scrape-off layer (SOL) simulation codes, such as SOLPS [1, 13], and by using simpler approximations derived from the Lengyel model [14–18]. Validating the predicted impurity con-

*Email address:* stuart.henderson@ukaea.uk (S. S. Henderson)

[1]See the author lists of B. Labit *et al.* 2019 Nucl. Fusion 59 086020 [2]H. Meyer *et al.* 2019 Nucl. Fusion 59 112014 and [3]E. Joffrin *et al.* 2019 Nucl. Fusion 59 112021

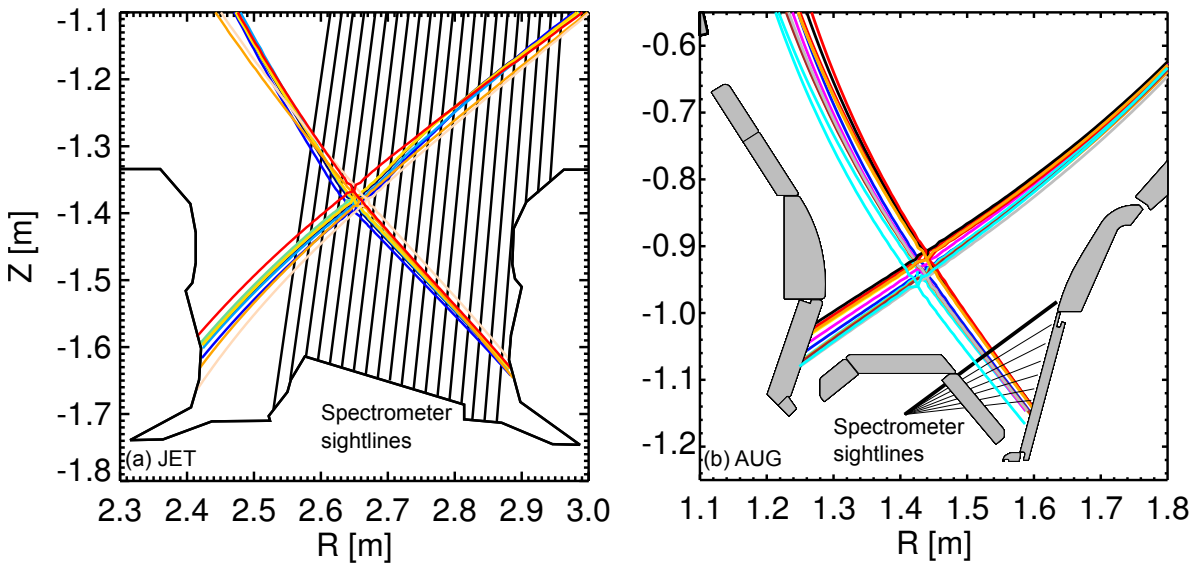


Figure 1: The last closed flux surface is shown for each shot used in the database. Divertor spectrometer sightlines on both (a) JET and (b) AUG are shown for reference.

centrations from these models in current devices is therefore of high importance and, recently, a method was developed to measure the N concentration, $c_N$, in the outer divertor of ASDEX Upgrade (AUG) using a new spectroscopic N II line ratio technique [19, 20]. Since these spectroscopic measurements are generally widely available, this paper builds on these studies to create a database of $c_N$ measurements in partially detached, H-mode plasma scenarios on both AUG and JET-ILW. This paper presents the first experimental assessment of $c_N$ in two, metal-walled tokamaks with vertical outer divertor configurations to demonstrate the key parameter dependences to reach detachment, including the scaling with the separatrix density $n_{e,sep}$ and the power flowing to the outer divertor $P_{div,outer}$.

The paper is structured as follows: section 2 and 3 presents the range of SOL parameters assessed in the database and an overview of the model used to measure $c_N$. The parameter dependencies from the database are described in section 4. An experimental scaling law for predicting the threshold $c_N$ required detachment is presented in section 5 including comparisons to equivalent theoretical scaling laws from 2P models. Finally, concluding remarks will be given in section 6.

## 2. Experimental database

The database used to assess the threshold outer divertor nitrogen concentration, $c_N$, required to reach detachment spans 13 pulses on AUG and 10 pulses on JET-ILW carried out between the years of 2013 – 2020. Each pulse has a phase of $N_2$ seeding during H-mode with a partially detached outer divertor. The detachment state of the outer divertor is assessed on AUG by using the real-time estimate of the outer divertor temperature, $T_{div}$, derived from shunt measurements [10]. On JET, both the roll-over of the ion saturation current and temperature estimate from Langmuir probe measurements in the outer divertor are used to estimate the detachment state [21]. Furthermore, since simulations show that the N II emission front is a good indicator for the poloidal location of the deuterium ionisation front [22], a combination of N II measurements from spectroscopy and filtered divertor camera images are used to verify the LP measurements on JET. Note that the $c_N$ are measured at detachment onset, rather than at full roll-over. The parameter dependences discussed in section 5 may be different if deeper detachment is required [23]. Lastly, the SOL conditions between JET and AUG have not been optimised in this database to produce similarity experiments [24]; however, on both machines, the outer divertor target is located on the vertical target as shown in figure 1.

The database includes a range of parameters: from AUG the data span $n_{e,sep} = 2 - 4 \times 10^{19}$ m$^{-3}$, $P_{sep} = 3.5 - 12$ MW, and $I_P = 0.8 - 1.20$ MA, and from JET $n_{e,sep} = 2.2 - 3.5 \times 10^{19}$ m$^{-3}$, $P_{sep} = 14 - 22$ MW, and $I_P = 2.5$ MA. On both machines, the elongation is $\kappa \approx 1.7$, while $a_{min} \approx 0.5$ and $a_{min} \approx 0.9$ on AUG and JET, respectively.

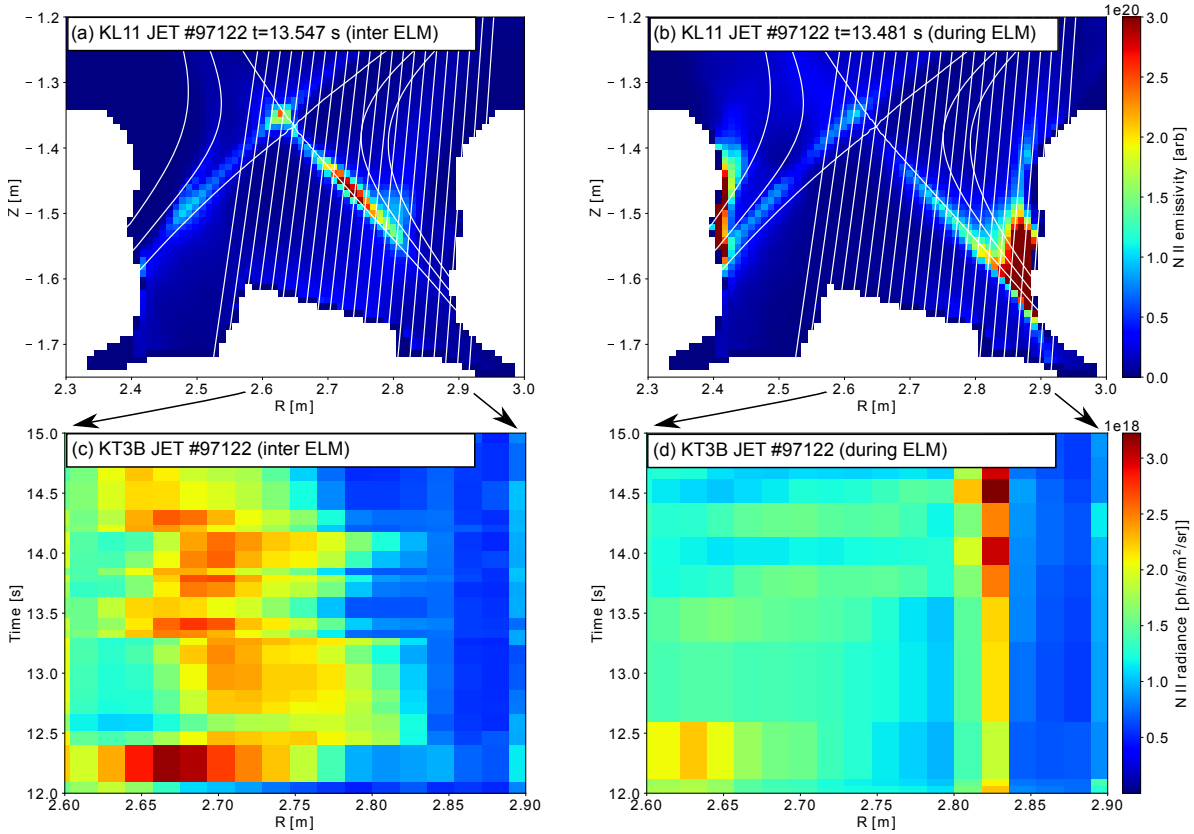


Figure 2: Tomographic inversions of the divertor camera images on JET, filtered to the narrow band-pass covering the N II emission at $\lambda \approx 500$ nm are shown for (a) an inter ELM and (b) ELM time frame during JET #97122. Note that the same colour scale is used in both (a) and (b) and has been artifically saturated to demonstrate the differences in poloidal location of the emission. The radiance of the N II line at $\lambda = 404.1$ nm from the divertor spectrometer measurements in the same pulse fitted during inter ELM and ELM time windows is shown in (c) and (d), respectively.

## 3. Divertor nitrogen concentration

The model for calculating $c_N$ is given by

$$c_N = \frac{4\pi I_{NII}}{(f_{N^+} PEC^{exc} + f_{N^{2+}} PEC^{rec})} \frac{1}{\Delta L n^2_{e,NII}}, \qquad (1)$$

where $I_{NII}$ is the N II radiance in $[ph/s/m^2/steradian]$, $\Delta L$ is the length of the N II emitting region through the line-of-sight (LOS) in $[m]$, $PEC^{exc,rec}$ are excitation and recombination photon emissivity coefficients [19] in $[m^3/s]$, $f_{N^z}$ is the fractional ion abundance of the $Z$ charged ion, and $n_{e,NII}$ is the electron density in $[m^{-3}]$ averaged through the LOS. The $f_{N^z}$ is calculated using a zero-transport ionisation balance. The assumption of zero-transport was tested in figure 7 of [19] and shown to be valid for temperatures measured below $\approx$ 4 eV. This is also discussed further in section 3.2.

### *3.1. Impact of ELMs*

The principle spectrometers used on AUG and JET are the Czerny Turner-like visible spectrometer [25] and the mirror-linked spectrometer [26], which have temporal resolutions of 400 Hz and 25 Hz, respectively. The sightline geometries for the JET and AUG spectrometers are shown in figure 1. The ELM frequencies on both machines are typically greater than 50 – 100 Hz. Where inter ELM measurements are not possible, it is crucial to assess the impact of the ELM on the N II radiance measurement.

Tomographic reconstructions of the filtered divertor camera images measured on JET [27], which take into account reflections, are used to assess the impact of ELMs in JET #97122 which has a sufficiently low ELM frequency. The inverted N II emission measured inter ELM and during the ELM is shown in figure 2a and b, respectively, where the same colour scale is used in both. During the inter ELM phase, the N II emission is located mid-way between the X-point and strike-point close to the separatrix. When the ELM occurs, the emission zone moves close to the target. For the vertical viewing geometry used by the divertor spectrometer,

this implies that the line-integrated radiance effected by ELMs will be in the radial range $R = 2.8-2.85$m, where $R$ is defined along the horizontal divertor target plate (tile 5). Therefore, the channels measuring $R \leq 2.8$ m are used to evaluate $c_N$.

On AUG, it was previously shown [19] that ELMs do not significantly change the intensity of the N II radiance measured through the AUG sightline shown in bold in figure 1b (referred to as channel ROV-14); however, the intensity measured through channels viewing closer to the strike-point are significantly increased during the ELM. This is consistent with the inverted images shown in figures 2a and b. Therefore, on AUG, although inter ELM data is taken wherever possible, the ROV-14 channel is used to avoid complications due to ELMs in discharges where inter ELM data is not available.

### 3.2. Temperature and density

The $c_N$ measurement is dependent on the temperature and density of the plasma associated with the N II emission, referred to as $T_{e,NII}$ and $n_{e,NII}$, respectively. The $T_{e,NII}$ and $n_{e,NII}$ drive the rate of excitation and recombination, while $c_N \propto 1/n^2_{e,NII}$. Measurements of the two spectroscopic line ratios used to determine $T_{e,NII}$ and $n_{e,NII}$ [19] are shown in figure 3; the time windows are limited on AUG to $T_{div} = 0 - 20$ eV and on JET to $t - t_{seed} = 1 - 2.5$ s. On average, the measured line ratios on both JET and AUG fall between the contours of constant temperature at $3 - 4$ eV. On JET, a significant proportion of the line ratios also indicate lower temperatures due to the inclusion of a sightline viewing close to the strike-point ($R = 2.8$ m). Additionally, the average line ratios for each sightline indicate a rise in $n_e$ towards the strike-point on AUG; while on JET $n_e$ remains relatively constant but $T_e$ observes a modest drop towards the strike-point.

When considering only atomic processes the N II emission is predicted to peak at $T_e \approx 3.5$ eV, consistent with the $T_{e,NII}$ measurements shown in figure 3. This indicates that cross-field and parallel transport are not significantly altering the N II emission profile in the outer divertor and that the zero-transport assumption made in equation 1 is valid.

### 3.3. Length of emission

$c_N$ in this paper assume that line-integration effects are negligible, and that the N II emission originates from a narrow, localised layer of plasma of constant $T_e$ and $n_e$ intercepting the spectrometer LOS. Furthermore, as described in equation 1, the model assumes that this thin layer of plasma can be simply described by a unit

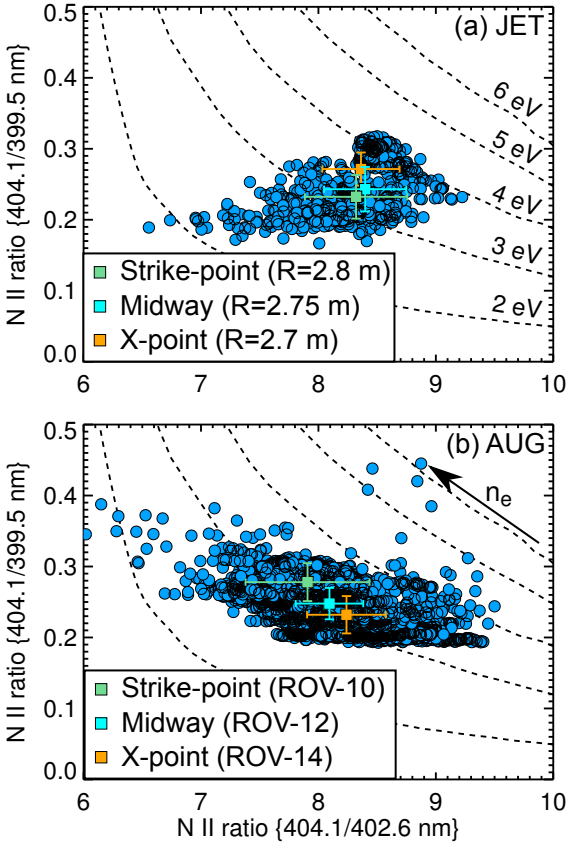


Figure 3: N II line ratios for each shot in the database for (a) JET measured between $t-t_{seed} = 1-2.5$ s and (b) AUG measured between $T_{div} = 0 - 20$ eV. The average ratios for each sightline are shown by the square symbols. Contours of $T_e$ calculated using the atomic rate coefficients are shown by dashed lines, with $n_e$ increasing from right to left in each figure.

length (i.e. $c_N \propto 1/\Delta L$). In the divertor configurations considered in this analysis, the N II emission between the X-point and the poloidal (upstream) location of the N II front are typically localised to a thin layer close to the separatrix located marginally within the SOL, rather than private flux location (PFR), as shown in figure 2a. However, due to the uncertainty in the equilibrium and inverted data, any distinction of the location between SOL and PFR should be treated cautiously. Conversely, the N II emission closer to the strike-point shows that the emission begins to spread across the SOL. Therefore, due to the localisation of the measurement and the negligible impact of ELM induced emission, only spectroscopic measurements between the front location and the X-point are used to infer $c_N$.

The emission profile through a divertor spectrometer LOS on JET, calculated using the data from the inverted camera image, is shown in figure 4a. For JET, $\Delta L = 7$

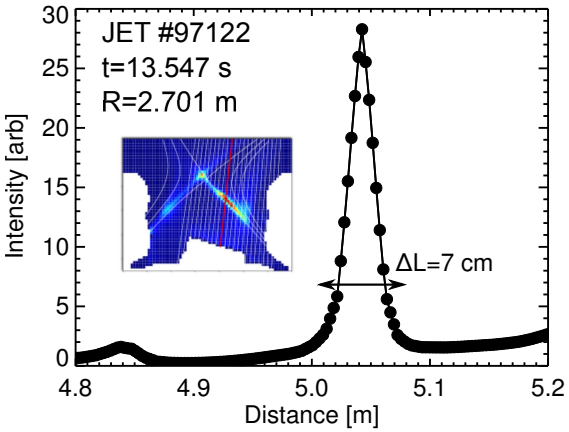


Figure 4: N II emission from a inverted divertor camera image showns as a function of the path length integral of the divertor spectrometer channel measuring at R=2.701 m for JET #97122 at t=13.547 s.

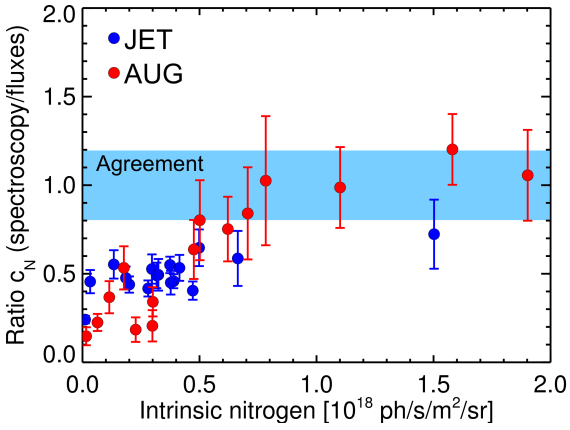


Figure 5: The ratio of $c_N$ measured from spectroscopy and valve fluxes is shown as a function of intrinsic nitrogen, estimated by using the N II radiance measured immediately before seeding.

cm is used to describe the emission region at the front location. Although 7 cm appears to be marginally wider than the width of the Gaussian, this difference should account for any additional contribution to the emission from the background. For each time step, the front location is calculated by finding the peak N II radiance measured by the divertor spectrometer across the radius (within $R \leq 2.8$ m). $\Delta L$ is reduced to 5 cm in sightline channels measuring further upstream towards the X-point.

Although the equivalent inverted images of N II are not available on AUG, similar behaviour of the emission is expected and observed in SOLPS modelling [13]. Therefore, $\Delta L$ is modelled as a function of $T_{div}$ as described in [19]. In this model, $\Delta L = 6$ cm at partial detachment (e.g. $T_{div} = 3 - 5$ eV).

### *3.4. Concentration measurements and uncertainties*

The spectrometer sightline geometries on both AUG and JET allow for $c_N$ measurements localised along the separatrix in the outer divertor. It is more convenient to consider one representative $c_N$ for the outer divertor in each shot when assessing the threshold $c_N$ for detachment. Therefore, the radial $c_N$ measurements on JET are averaged over three radial channels between the front location and the X-point. On AUG, as discussed in the sections above, the ROV-14 sightline channel measurements are used to represent the outer divertor $c_N$. The $c_N$ are then averaged over $T_{div} = 3-5$ eV and $t-t_{seed} = 1-2$ s on AUG and JET, respectively.

There are two main sources of uncertainty in the measured $c_N$: the $T_{e,NII}$ and $n_{e,NII}$ predicted from line ratios and the $\Delta L$ model. The impact of reflections from the metal wall is less significant on AUG as the spectrometer sightlines end in viewing dumps. On JET, reflections are expected to increase the N II emission by $< 15\%$ [27].

The uncertainty of $T_{e,NII}$ and $n_{e,NII}$ are caused by the quality of the spectral fits; the quality of the atomic data is discussed in [19]. On AUG, the typical errors on the 404.1/399.5 nm and 404.1/402.6) nm N II line ratios, called LR1 and LR2, are $\approx 1\%$ and $\approx 2\%$, respectively. This propagates to an uncertainty of $\approx 10\%$ on $T_{e,NII}$ and $n_{e,NII}$, which subsequently produces an overall $c_N$ uncertainty of $\approx 20 - 30\%$. Furthermore, in pulses with low $N_2$ seeding, the N II line at $\lambda = 402.6$ nm is two orders of magnitude weaker than the $\lambda = 399.5$ nm N II line and is often blended with another line (thought to be from F II). In these scenarios, the $T_{e,NII}$ is approximated to be $3.1 - 3.5$ eV which can lead to higher $c_N$ uncertainties of $30 - 40\%$. Overall, these uncertainties outweigh those from the $\Delta L$ model. In principle, this error could be reduced if the spectral radiance was averaged over more than one frame to improve the statistics.

LR1 and LR2 have significantly lower uncertainties from JET measurements ($\leq 0.3\%$) and generate a modest uncertainty of $\approx 5\%$ on $c_N$. This is mainly due to better statistics on the measured spectral radiance (likely caused by the longer integration time). Therefore, the leading uncertainty on JET is driven by the averaging of $c_N$ over the three radial channels. The authors assume the uncertainty associated with the absolute calibration of the diagnostic and window transmission is negligible in comparison to these leading order uncertainties described above.

Finally, the measured $c_N$ from JET and AUG can be

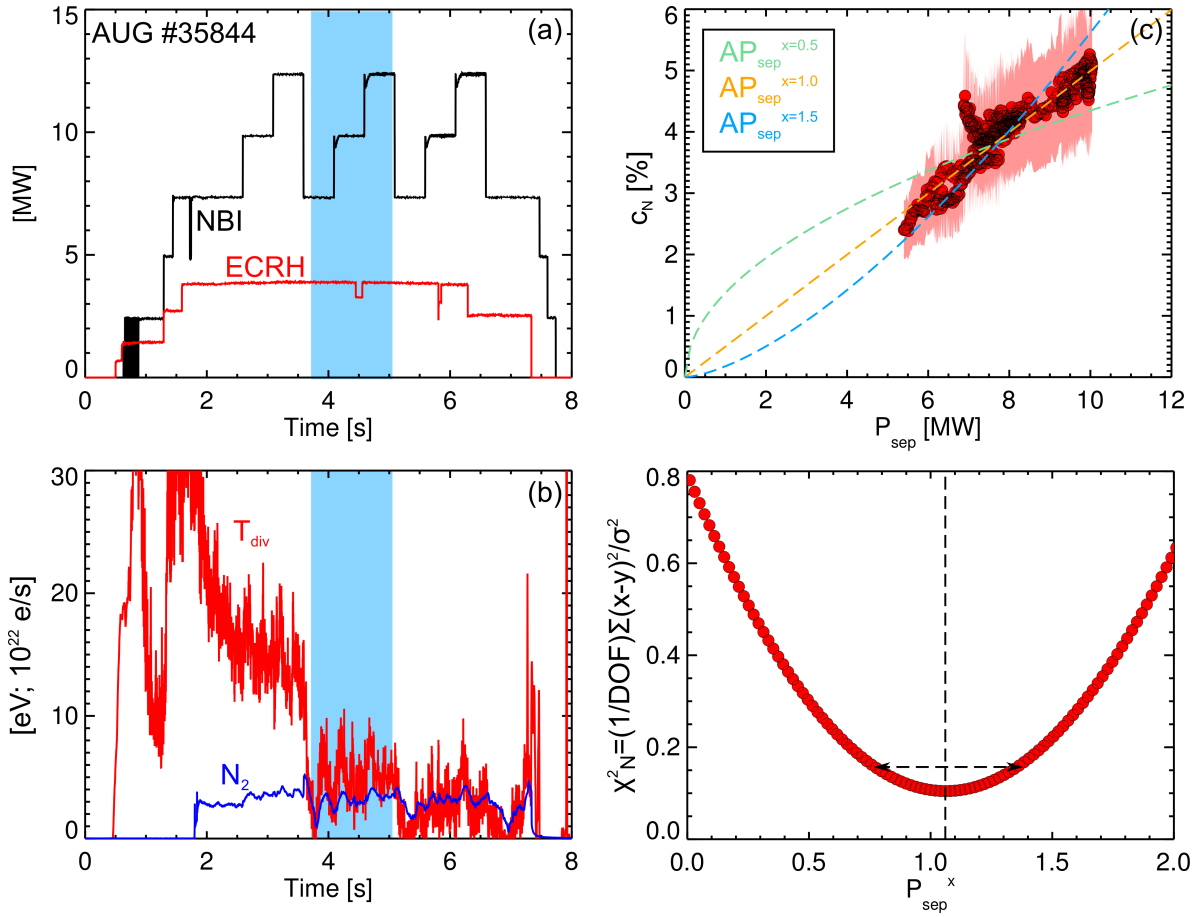


Figure 6: The NBI and ECRH input powers are shown in (a) for AUG #35844 with the corresponding $T_{div}$ and $N_2$ seeding rate shown in (b) as a function of time. The measured $c_N$ is shown as a function of $P_{sep}$ in (c) during the time window shown by the blue shaded region in (a) and (b). The reduced $\chi^2_N$ for different $AP^x_{sep}$ fits are shown in (d).

compared to estimates of $c_N$ based on the ratios of the gas valve fluxes,

$$c_{N,flux} = \frac{\Gamma_{N2}/7}{(\Gamma_{D2} + \Gamma_{N2}/7)} \quad (2)$$

where $\Gamma_{N2}$ and $\Gamma_{D2}$ are the impurity and main ion gas valve fluxes. Comparisons of the two measurements are shown in figure 5 as a function of the intrinsic nitrogen content in the machine which is approximated by the N II radiance measured before the seeding valve is opened. In stationary scenarios with high measured intrinsic N II radiance, indicative of fully saturated vessel surfaces, the measurements agree on AUG; however, when the intrinsic N II radiance is low, the two measurements can differ by an order of magnitude. On JET, a similar but less pronounced trend is found, with ratios remaining around 0.5 in most pulses. This could be due to the seeding recipe on JET, which typically injects a large amount of $N_2$ for a short time window at the start of injection, before reducing to the requested amount. This large initial influx of $N_2$ may be an effective technique for rapidly saturating the vessel walls, and therefore ensuring that the N concentration reaches a steady state value that is repeatable in different pulses, regardless of the machine conditions prior to seeding.

## 4. Parameter dependences

In principle, any regression analysis should include all parameters that are varying across the database. The choice of parameter dependencies in this analysis, noted in section 2, have been guided by theoretical scaling laws (see section 5). Other unknown parameters may be affecting the measured $c_N$ required for detachment; for example, the divertor connection length, the parallel transport, and the strike-point position (or divertor

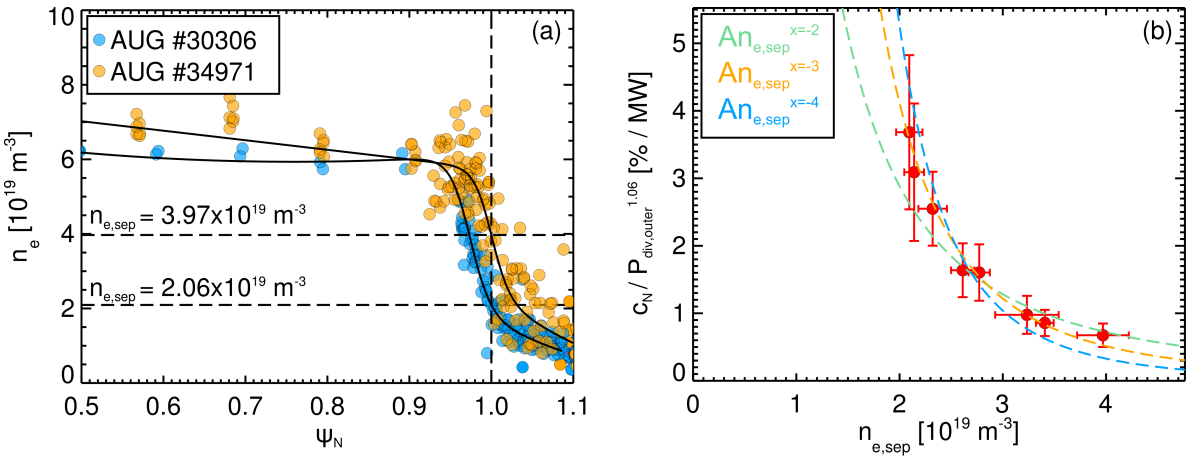


Figure 7: Fits of inter ELM $n_e$ are shown for two AUG shots, #30306 and #34971. The AUG $c_N/P_{div,outer}^{1.06}$ at constant $I_P = 0.8$ MA are shown as a function of $n_{e,sep}$ in (b) along with fits to $An_{e,sep}^x$ for $x = -2, -3, -4$.

closure). While the changes in these parameters across the database are expected to be modest, their impact on the derived threshold $c_N$ for detachment cannot be ruled out.

### 4.1. SOL power

The power crossing the separatrix is defined as $P_{sep} = P_{input} - P_{main} - dW/dT$, where $P_{input}$ is the total input power, $P_{main}$ is the radiated power measured by bolometry in the main chamber volume, and $W$ is the stored energy. Since this analysis focuses solely on the scaling of detachment in the outer divertor, a fraction of $P_{sep}$ is used in the scaling according to an in-out power asymmetry of $1:2$ and a fraction $1 - 1/e$ which is lost either to the wall or to the divertor SOL outside the first power width flux tube [16]. This leads to a corrected power entering the outer divertor defined as $P_{div,outer} = P_{sep}/\alpha$ where $\alpha = 2.37$. On JET, $\alpha$ can be measured by comparing $P_{sep}$ integrated over the duration of a pulse and the corresponding thermocouple tile energies covering the vertical outer divertor tiles. Considering only the pulses used in this database, the measured value is $\alpha = 2.26 \pm 0.12$. For consistency, the $\alpha = 2.37$ is used to scale $P_{sep}$ on AUG and JET.

The AUG #35844 discharge is used to demonstrate the $P_{div,outer}$ dependency on the threshold $c_N$ required for detachment. This pulse varies the $P_{input}$ to three different levels, whilst keeping the $N_2$ seeding valve on feedback to $T_{div} = 5$ eV as shown in figures 6a and b. The $c_N$ is shown as a function of $P_{sep}$ in figures 6c, with the best fit of the function $AP_{sep}^x$ to the $c_N$ determined as $c_N \propto P_{div,outer}^{1.06\pm0.28}$ where the error is taken as the width of the reduced $\chi_N^2 = 1/DOF \sum_i (x_i - y_i)^2/\sigma_i^2$ within 50% of the minimum $\chi_N^2$ as shown in figure 6d.

While the database of $c_N$ should act to verify this scaling over a wide range of $P_{sep}$ on both machines, the advantage of assessing the dependency in the experiment shown above is that the plasma conditions stay relatively constant during the changes in $P_{sep}$.

### 4.2. Separatrix density

There are no experiments that scan only $n_{e,sep}$ at constant $T_{div}$, therefore the database of $c_N$ from AUG at constant $I_p = 0.8$ MA are selected to assess the $n_{e,sep}$ parameter dependency. The $P_{div,outer}$ are not constant for these data, therefore $c_N^{norm} = c_N/P_{div,outer}^{1.06}$ is used to account for any changes in $P_{div,outer}$, where the total uncertainty is defined as $\Delta c_N^{norm}/c_N^{norm} = \sqrt{(1.06\Delta P_{div,outer}/P_{div,outer})^2 + (\Delta c_N/c_N)^2}$. Note that this does not account for the $P_{div,outer}$ exponent uncertainty.

The fits to the inter ELM $n_e$ profiles across the core plasma radius are shown in figure 7a for the two data points providing the highest and lowest $n_{e,sep}$. The fits are shifted to match the separatrix temperature, $T_{e,sep}$, evaluated from the scaling laws described in [29]. The uncertainty in $n_{e,sep}$ is taken as the standard deviation of the fit from $\psi_N = 0.995 - 1.005$ to account for the $n_{e,sep}$ gradient steepness near the separatrix. The normalised $c_N$ is shown as a function of $n_{e,sep}$ in figure 7b, with the best fit of the function $An_{e,sep}^x$ determined as $c_N/P_{div,outer}^{1.06} \propto n_{e,sep}^{-2.67\pm0.27}$.

### 4.3. Plasma current and minor radius

Most data from AUG are at $I_P = [0.8, 1.0]$ MA with only one point at $I_P = 1.2$ MA. Similarly, all the data

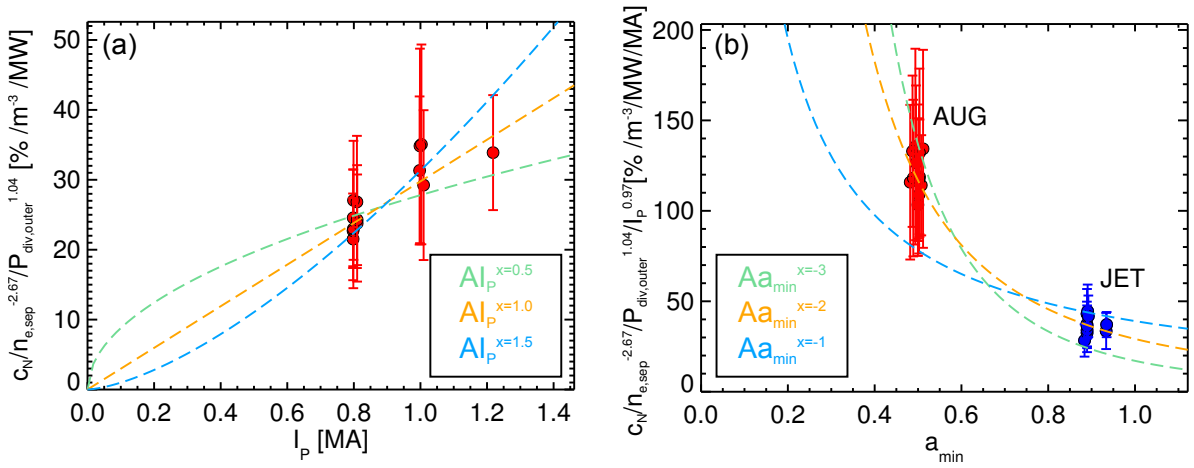


Figure 8: The AUG $c_N/n_{e,sep}^{2.67}/P_{div,outer}^{1.06}$ measurements are shown as a function of $I_P$ in (a) along with fits to $AI_P^x$ for $x = 0.5, 1.0, 1.5$. Taking $I_P^{0.97}$ as the best fit to the data in (a), the corresponding $c_N/n_{e,sep}^{2.67}/P_{div,outer}^{1.06}/I_P^{0.97}$ from the full database, including AUG and JET data, are shown as a function of $a_{min}$ in (b), along with fits to $Aa_{min}^x$ for $x = -1, -2, -3$.

from JET are at constant $I_P = 2.5$ MA. Therefore, the AUG database provides only a tentative assessment of the $I_P$ parameter dependency. Ideally, the $I_P$ dependency should be assessed over a a wider range of $I_P$ (the JET data increases this range to $I_P = 2.5$ MA, but $a_{min}$ is also changing).

Using the $c_N$ from the AUG database and normalising them to $c_N^{norm1} = c_N/P_{div,outer}^{1.06}/n_{e,sep}^{-2.67}$, the dependency with $I_P$ is shown in figure 8a. The $\chi_N^2$ analysis provides the best fit with $c_N^{norm1} \propto I_P^{0.97\pm0.36}$; the larger uncertainty on the exponent is consistent with requiring data over a greater range of $I_P$.

Finally, the entire database of measured $c_N$ from AUG and JET are normalised by $c_N^{norm2} = c_N/P_{div,outer}^{1.06}/n_{e,sep}^{-2.67}/I_P^{0.97}$ and shown as a function $a_{min}$ in figure 8b. Although the $a_{min}$ changes by a factor of two, ideally the parameter dependency should be assessed over at least three different values. Including divertor concentrations from Alcator C-Mod and DIII-D (with an assessment of the radiation contribution from the intrinsic carbon) could provide a more robust assessment of the $a_{min}$ scaling. The $\chi_N^2$ analysis produces the best fit with $c_N^{norm2} \propto a_{min}^{-1.99\pm0.25}$.

## 5. Assessment of scaling law

Taking each parameter dependency from the previous subsections gives a final scaling law defined as:

$$c_{N,regress} = 29.9 P_{div,outer}^{1.06\pm0.28} n_{e,sep}^{-2.67\pm0.27} I_P^{0.97\pm0.36} a_{min}^{-1.99\pm0.25} (1+\kappa^2)^{-1} \quad (3)$$

where $P_{div,outer}$ is in [MW], $n_{e,sep}$ in [$10^{19}$ m$^{-3}$] and $I_P$ in [MA]. The comparison of the scaling law in equation 3 to the measured $c_N$ is shown in figure 9a. While the dependency with $(1+\kappa^2)^{-1}$ is not varied in the database, it is maintained in equation 3 for clarity; it is effectively only acting as an additional scaling factor.

Scaling laws by Kallenbach (equation 9 [28]), Post and Reinke (equation 7 [15] and equation 8 [17]), and Goldston (equation 9 [18]) have all been derived based on the model described by Lengyel [14]. Note that the analysis below doesn't consider the extended model proposed by Reinke (equation 10 [17]) as the majority of pulses in this database are far above the L-H threshold power. These derivations are given as

$$c_{N,Kallenbach} = 1.3 P_{div,outer} R_{maj}^{-1} f_Z^{-1} p_0^{-1} (\lambda_{int}/0.005)^{-1} (R_{maj}/1.65)^{-0.1} \quad (4)$$

$$c_{N,(Post,Reinke)} = 0.5 q_\parallel^2 \kappa_0^{-1} n_u^{-2} T_u^{-2} L_{INT}^{-1} \quad (5)$$

and

$$c_{N,Goldston} = 18.3 P_{div,outer} n_{e,sep}^{-2} I_P a_{min}^{-3} (1+\kappa^2)^{-1} \quad (6)$$

where $p_0$ is the divertor pressure, $\lambda_{int}$ is the broadened power width, $R_{maj}$ is the major radius, $q_\parallel$ is the parallel heat flux (calculated using equation 2 [17]), $n_u$ is the upstream density (proportional to $n_{e,sep}$), $T_u$ is the upstream temperature, and $L_{INT}$ is the integral of the radiative cooling function along the SOL multiplied by $\sqrt{T_e}$. The same transport (i.e. $n_e\tau$) is assumed here as in [17]. The divertor pressure is estimated on both AUG

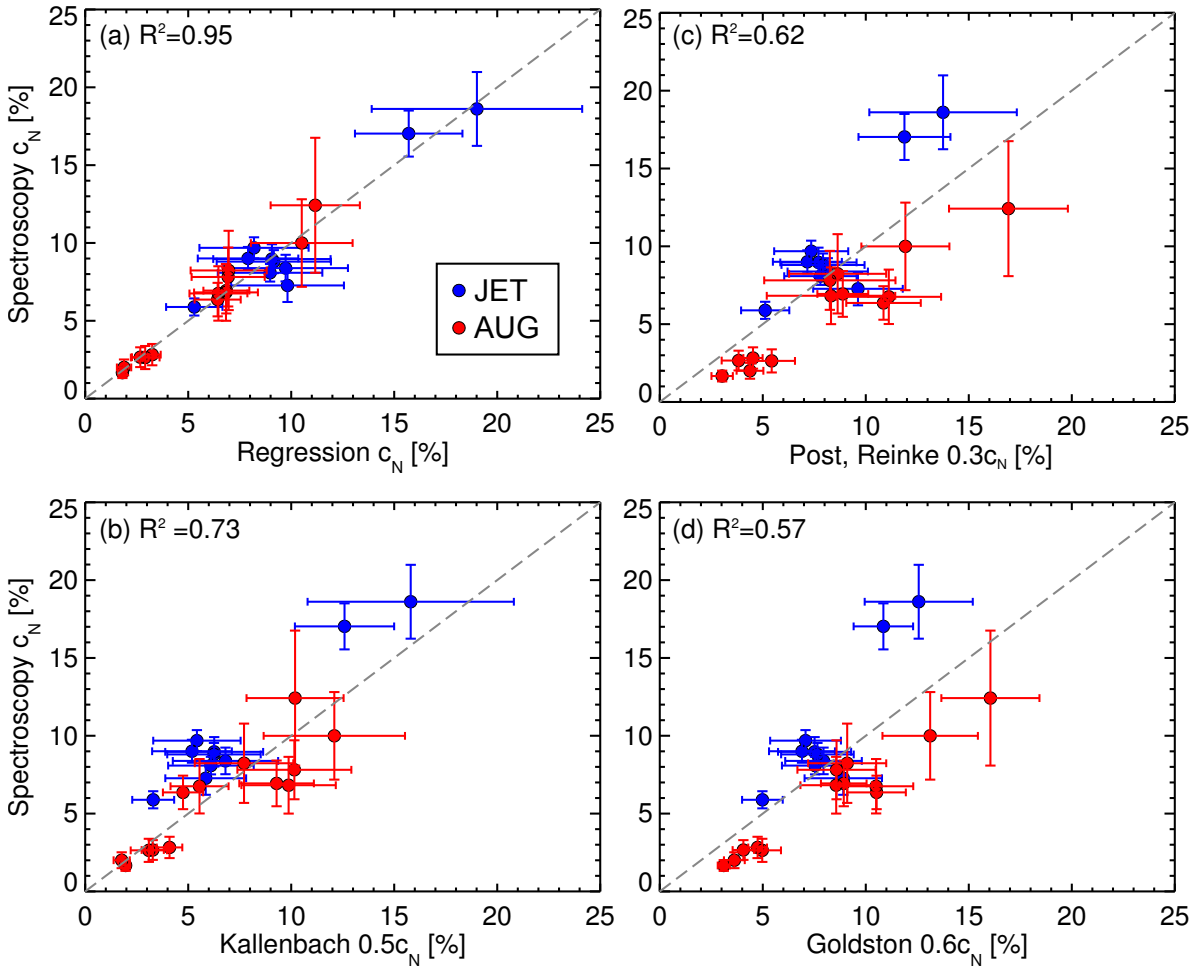


Figure 9: The database of $c_N$ are shown as a function of (a) the regression given in equation 3 and as a function of the scaling laws derived by (b) Kallenbach [28] (c) Post and Reinke [15, 17] and (d) Goldston [18]. The blue and red points indicate data from JET and AUG, respectively.

and JET using $p_0 = (n_{e,sep}/2.65)^{3.22}$; however, this scaling law has only been verified on AUG [28]. $c_{N,Goldston}$ is written as a function of $I_P$ by substituting the expressions for $B_p$ and $f_{GW,sep}$, with the factor 18.3 derived from a normalisation to $c_{N,Kallenbach}$.

The comparisons with $c_{N,Kallenbach}$, $c_{N,(Post,Reinke)}$ and $c_{N,Goldston}$ are shown in figures 9b, c and d, respectively. In each case, the scaling laws are multiplied by a factor to produce the best match to the experimental $c_N$. Unsurprisingly, both $c_{N,Kallenbach}$ and $c_{N,Goldston}$ are reduced by a similar factor $\approx 0.5-0.6$; however, $c_{N,(Post,Reinke)}$ requires a stronger reduction factor of 0.3. Since the modelled values shown in figure 9 are derived using $P_{div,outer}$ as an input, rather than $P_{sep}$, the factor $\approx$ 2.5 overestimate of $c_{N,(Post,Reinke)}$ suggested by Reinke [17] is already accounted for. Furthermore, it has recently been shown that the Ne concentrations taken at the detachment onset from a database of ITER baseline SOLPS4-3 simulations are lower than the Lengyel model predictions by a factor of $\approx$ 0.25 [30]; a scaling factor very similar to that found in this analysis.

While $c_{N,Kallenbach}$ and $c_{N,Goldston}$ both predict a linear scaling with $P_{div,outer}$, $c_{N,(Post,Reinke)}$ suggests a moderately stronger dependence of $P_{div,outer}^{8/7}$ (by using $T_U \propto q_{\|}^{2/7}$ and $L_{INT} \propto T_U$). Both predictions are consistent within the uncertainty of the exponent inferred from the experiment. The experimental $c_N$ suggest a stronger dependence on $n_{e,sep}$, with an exponent of $-2.67 \pm 0.27$ compared to an exponent of -2 predicted by both $c_{N,(Post,Reinke)}$ and $c_{N,Goldston}$. However, this stronger dependence on $n_{e,sep}$ gives better agreement with $c_{N,Kallenbach}$ considering that $p_0 \propto n_{e,sep}^{3.22}$ as described above.

Overall, the $c_{N,Kallenbach}$ model gives the closest

agreement to experiment, with $R^2 = 0.73$ compared to 0.62 and 0.57 for $c_{N,(Post,Reinke)}$ and $c_{N,Goldston}$, respectively. The $c_{N,(Post,Reinke)}$ and $c_{N,Goldston}$ could effectively be separated into two branches for JET and AUG. This is effectively accounted for in $c_{N,regress}$ by the weaker dependence on $a_{min}^{-1.99\pm0.25}$ compared to $a_{min}^{-3}$. However, without data at a third value of $a_{min}$ this result requires futher verification. Furthermore, the $c_{N,(Post,Reinke)}$ and $c_{N,Goldston}$ values shown in figure 9 have been calculated with constant parallel transport ($n_e\tau$) which, although not an unreasonable assumption, merits further investigation. Conversely, better agreement with $c_{N,Kallenbach}$ indicates consistency with the weak scaling of $R_{maj}$.

Uncertainties in the measurements can also not be discounted when considering machine size scaling; however, to have any impact they must be systematic to one machine only. For example, uncertainty in the atomic data would lead to the same systematic change of $c_N$ on both machines and would not change the size scaling. Conversely, inaccuracies of $\Delta L$, $P_{div,outer}$ or $n_{e,sep}$ on one machine, but not the other, could change the scaling with $a_{min}$.

## 6. Conclusions

A database of experimental nitrogen concentrations measured in the outer divertor on JET and AUG during $N_2$ seeded H-mode scenarios and averaged during periods of partial detachment have been compared against the power flowing to the outer divertor, the separatrix density, the plasma current, and the minor radius. The database demonstrates that the threshold nitrogen concentration scales as $P_{sep}^{1.06\pm0.28} n_{e,sep}^{-2.67\pm0.27} I_P^{0.97\pm0.36} a_{min}^{-1.99\pm0.25}$. The near-linear scaling with $P_{sep}$ is consistent with predictions from the Lengyel model; however, the data indicates a moderately stronger dependence on $n_{e,sep}$. While the scaling with $P_{sep}$ and $n_{e,sep}$ have been tested over a wide range of data across both JET and AUG, the scaling with $I_P$ and $a_{min}$ should be treated cautiously until more data is added to the database. Future experiments should address the effect of different neutral closures, for example examining the differences between a vertical and horizontal outer target configuration on JET. In addition, combining these new divertor concentration measurements with equivalent core charge exchange measurements will provide an assessment of the impurity enrichment. Finally, a promising set of Ne II lines have been identified in the visible spectrum along with accompanying atomic data which could facilitate testing of the impurity species dependency of the threshold concentration required for detachment.


## Acknowledgements

This work has been carried out within the framework of the EUROfusion Consortium and has received funding from the Euratom research and training programme 2014-2018 and 2019-2020 under grant agreement No 633053 and from the EPSRC [grant number EP/T012250/1]. The views and opinions expressed herein do not necessarily reflect those of the European Commission.


## References


[1] R. A. Pitts *et al.*, J. Nucl. Mater. **20**, 100696 (2019).
[2] E. A. Lazarus *et al.*, Nucl. Fusion **25**, 135 (1985).
[3] A. Kallenbach *et al.*, Nucl. Fusion **35**, 1231 (1995).
[4] J. Rapp *et al.*, Nucl. Fusion **44**, 312 (2004).
[5] J. A. Goetz *et al.*, Phys. Plasmas **6**, 1899 (1999).
[6] M. Komm *et al.*, Nucl. Fusion **59**, 106035 (2019).
[7] J. R. Harrison *et al.*, Plasma Phys. Control. Fusion **61**, 065024 (2019).
[8] J. A. Goetz *et al.*, J. Nucl. Mater. **266**, 354 (1999).
[9] M. Groth *et al.*, Nucl. Fusion **42**, 591 (2002).
[10] A. Kallenbach *et al.*, Nucl. Fusion **55**, 053026 (2015).
[11] M. Bernert *et al.*, 3rd IAEA Technical Meeting on Divertor Concepts, Vienna (Austria) (2019).
[12] T. Ravensbergen *et al.*, Nucl. Fusion **60**, 066017 (2020).
[13] F. Reimold *et al.*, J. Nucl. Mater. **463**, 128 (2015).
[14] L. L. Lengyel, IPP Report–1/191 (1981).
[15] D. Post, N. Putvinskaya, F. W. Perkins, and W. Nevins, J. Nucl. Mater. **220-222**, 1014 (1995).
[16] A. Kallenbach *et al.*, Plasma Phys. Control. Fusion **58**, 045013 (2016).
[17] M. L. Reinke, Nucl. Fusion **57**, 034004 (2017).
[18] R. J. Goldston, M. L. Reinke, and J. A. Schwartz, Plasma Phys. Control. Fusion **59**, 055015 (2017).
[19] S. S. Henderson *et al.*, Nucl. Fusion **58**, 016047 (2018).
[20] S. S. Henderson *et al.*, J. Nucl. Mater. **18**, 147 (2019).
[21] C. Giroud *et al.*, Plasma Phys. Control. Fusion **57**, 035004 (2015).
[22] A. E. Jaervinen *et al.*, J. Nucl. Mater. **463**, 135 (2015).
[23] B. Lipschultz, F. I. Parra, and I. H. Hutchinson, Nucl. Fusion **56**, 056007 (2016).
[24] S. Wiesen *et al.*, 1st IAEA Technical Meeting on Divertor Concepts, Vienna (Austria) (2015).
[25] S. Potzel *et al.*, Plasma Phys. Control. Fusion **56**, 025010 (2014).
[26] A. Meigs *et al.*, Rev. Sci. Instrum. **81**, 10E532 (2010).
[27] J. Karhunen *et al.*, Rev. Sci. Instrum. **90**, 103504 (2019).
[28] A. Kallenbach *et al.*, Plasma Phys. Control. Fusion **60**, 045006 (2018).
[29] H. J. Sun *et al.*, Plasma Phys. Control. Fusion **59**, 105010 (2017).
[30] D. Moulton, P. C. Stangeby, X. Bonnin, and R. A. Pitts, Nucl. Fusion **submitted**, (2020).